International Journal of Hydrogen Energy 58 (2024) 668–677

Contents lists available at ScienceDirect

International Journal of Hydrogen Energy

journal homepage: www.elsevier.com/locate/he

Cushion gas effects on clay-hydrogen-brine wettability at conditions relevant to underground gas storage

Azeezat Ali [a], David R. Cole [b], Alberto Striolo [a,c,*]

[a] Department of Chemical Engineering, University College London, London, WC1E 6BT, United Kingdom
[b] School of Earth Sciences, The Ohio State University, Columbus, OH, 43210, USA
[c] School of Sustainable Chemical, Biological and Materials Engineering, The University of Oklahoma, Norman, OK, 73019, USA

ARTICLE INFO

Handling Editor: Prof B Shabani

ABSTRACT

Geological storage of hydrogen, and its retrieval as needed, could play a vital role in the transition from fossil-fuel based energy to clean renewable energy production. Cushion gases, such as carbon dioxide and methane, can be used to maintain the reservoir pressure required to increase the efficiency of injection and extraction processes. Because water is ubiquitous in the subsurface, it can provide additional sealing mechanisms and affect the ability of gases to penetrate porous rocks. Because the interactions among the various gases and the wetting properties in the subsurface affect the sealing capacity of the caprock, they can provide important considerations for the proper design of geological storage and retrieval processes. Molecular dynamics simulations were used to evaluate the effects of varying compositions of cushion gases (CO_2 and CH_4) on brine-hydrogen-kaolinite clay wettability. Contact angles and liquid–gas interfacial tension were computed for 10% NaCl brines at 323 K and pressures in the range 5–40 MPa. These conditions are representative of underground gas storage. The results showed that, in pure H_2, the kaolinite siloxane surface is 'intermediate wet', with contact angles ranging from 91° to 106°. At constant temperature and pressure, CO_2 and CH_4 cause the surface to become less water-wet, yielding larger contact angles. We observed that CO_2 led to a more significant increase in contact angles. This suggests that CO_2 or CH_4 lead to easier recovery of hydrogen. These cushion gases also reduce gas-brine interfacial tensions, with CH_4 yielding a less pronounced effect than CO_2. Reductions in interfacial tension translate to reduced capillary sealing pressure, which implies that hydrogen can be retrieved at lower pressures. The results presented suggest that the efficiency of a gas used as cushion gas is related to the density difference between the resultant gas mixture and water. At the conditions tested here, CO_2 and CH_4 are found to reduce the sealing capacity of kaolinite towards hydrogen storage, while they are likely to improve hydrogen recovery. This should be taken into consideration when intermittent hydrogen storage is attempted in geological repositories.

1. Introduction

Advancements in large-scale storage technologies will contribute to the transition towards a low-carbon economy. For example, owing to daily and seasonal fluctuations, excess renewable energy (wind/solar) can be converted to green hydrogen by water electrolysis [1]. Hydrogen is an attractive energy storage option because of its high specific energy capacity [2]. However, its low density at standard conditions poses hurdles for transport and storage. Therefore, large volumes of H_2 are likely needed to be stored intermittently in underground geological formations, such as in depleted oil/gas reservoirs, deep saline aquifers, coal beds, salt and limestone caverns, tight gas formations, and organic-rich shale reservoirs [3,4]. The stored H_2 can then be extracted and converted to electricity, for example, when there is an increase in demand [4].

The feasibility of Underground Hydrogen Storage (UHS) is highly dependent on, among other factors, mineral surface wettability, rock-fluid and fluid-fluid interfacial tension (IFT), fluid density, solubility and gas diffusivity. These properties are significantly affected by conditions such as temperature, pressure, salinity, organic acid contamination [4], as well as gas pressure and composition. In addition, because water is ubiquitous in the subsurface, it can provide additional sealing capability as well as affect the transport of gases and their ability to infiltrate the rock mass [5]. Therefore, to effectively store H_2, it is

---

[*] Corresponding author. Department of Chemical Engineering, University College London, London, WC1E 6BT, United Kingdom.
E-mail address: astriolo@ou.edu (A. Striolo).

https://doi.org/10.1016/j.ijhydene.2024.01.151
Received 30 August 2023; Received in revised form 23 December 2023; Accepted 13 January 2024

essential to quantify, understand, and ultimately control how gas-rock-water interactions change in the subsurface and how they depend on environmental conditions. Because wettability describes the balance of interfacial interactions in three-phase systems, contact angles are frequently used to measure this important property [6,7].

Recently, experimental measurements have been reported for water/brine contact angles on mineral surfaces in the presence of hydrogen [8–22]. Ali et al. [20], e.g., showed that mica transitions from 'intermediate wet' to weakly 'water-wet' at high temperatures and low pressures. The increase in contact angles with pressure was attributed to the increase in the intermolecular interactions between hydrogen and the mineral surface, while increasing the temperature led to a reduction in the gas density [20,23]. In comparison to mica, the contact angles on quartz are lower, indicating that quartz is more hydrophilic than mica. Similar results concerning the effects of pressure on hydrogen wettability on clays are reported by Al-Yaseri et al. [22].

Among the experimental observations, a possible inconsistency is that contact angles for the mica/H_2/brine system decreased with increasing temperature, while those for the quartz/H_2/brine system increased with temperature. It is possible that this difference is related to the structure of the mineral surfaces. On quartz, water can form hydrogen bonds with the silanol groups of the surface, which become weaker as temperature increases, highlighting that the contact angle on mica depends on H_2 density, while on quartz, it depends on hydrogen bonding [20,21,24]. Iglauer et al. [17] observed similar results in their experimental work, where increasing pressure and temperature changed the sandstone surfaces from weakly 'water-wet' to 'intermediate wet'. Contrary to widely reported literature data, Hashemi et al. [19] found that there was no distinct correlation in the contact angles measured on a sandstone, within temperature and pressure ranges 20–50 °C and 20–100 bar, respectively. The authors attributed their results to differences in measurement methods and experimental conditions. Through geochemical modelling, Zeng et al. [16] linked the geochemical reactions taking place on gas-brine-rock interfaces to the wettability of the surface, and found that on carbonate rocks, increased temperature enhances the hydrophilicity of the surface due to greater repulsive force between H_2 and calcite. In general, the results from geochemical modelling corroborates the experimental (tilted plate method) results of Hosseini et al. [18] on the hydrogen wettability of carbonate formations at similar conditions.

Another important consideration pertains to observations regarding the water/brine-gas interfacial tension (IFT), which can be evaluated as follows [25]:

$$\gamma = \frac{\Delta\rho g}{\left(\beta k_{apex}\right)^2} \tag{1}$$

In Eq. (1), $\Delta\rho$ is the density difference between water/brine and gas, g is the gravitational acceleration, k_{apex} is curvature at the drop's apex, and β is a dimensionless shape parameter.

Several studies quantified water/brine-H_2 IFT [26–30], generally showing that the brine-H_2 IFT reduces linearly with increasing temperature and pressure, although temperature had a more significant effect. The IFT reduction with pressure is attributed to the increase in density of the compressed gas because liquid water is relatively incompressible. The substantial reduction in the density difference between water and hydrogen gas was considered responsible for the IFT decrease with rising temperature. Hosseini et al. [26] developed an empirical equation to predict IFT as a function of temperature, pressure, and brine molarity, achieving good agreement with experimental data. However, Chow et al. [28] found that at 298 K and 323 K, there is an initial increase in H_2-water IFT (from the surface tension value of water) with increasing pressure (up to ~ 2 MPa) before the IFT decreases linearly with further increases in pressure.

Rock-fluid IFT can be estimated via the Young's equation [i.e., Eq. (2)] and Neumann's equations of state. For example, in shale, rock-H_2 IFT was found to decrease with pressure and temperature. On the other hand, rock-water IFT decreases with temperature and remains constant with pressure because water is incompressible. This suggests that rock-gas IFT is the main parameter affecting the change in wettability with pressure in rocks [31]. These results can be correlated with the cohesive energy density (CED) of the different phases. For example, as pressure increases, the CED of the gas increases while the CED of the rock remains relatively constant. This yields a reduction in the difference between the rock and gas CED, which leads to favourable interactions between the gases and the rock. Similar findings were reported for H_2 and CO_2 on calcite. However, the calcite-gas IFT increased with temperature, which shows that rock-gas IFT depends on the gas type [32]. As the temperature increased, the gas CED decreases while the rock CED remains relatively constant, resulting in an increase in the rock-gas CED difference. This suggests less favourable interactions of the gases with calcite at elevated temperatures. Because the density of CO_2 decreases to a greater extent than H_2 density, the extent of increase in rock-gas IFTs is larger in CO_2/water systems than in H_2/water systems [32]. Arif et al. [33] also investigated solid/CO_2 and solid/water interfacial energies for quartz, mica, and coals. They reported that solid/CO_2 IFTs decreased with pressure and increased with temperature for the reasons explained above. Solid/water IFT decreased with temperature for all the minerals except for quartz where an increase was observed. The IFTs were correlated with the hydrophilicity of the surface, which allows the wetting behaviour to be understood. The increase in quartz/water IFT with temperature was attributed to desorption of water molecules from the surface. Another study showed that rock-water IFT increase with temperature on calcite, dolomite, quartz and shale for similar reasons [34], whereas the IFT of basalt and gypsum are unaffected by temperature. On the other hand, rock-H_2 IFT was found to decrease with pressure.

The Young's equation relates IFTs to contact angles as follows [35]:

$$\cos(\theta) = \frac{\gamma_{sg} - \gamma_{sw}}{\gamma_{wg}} \tag{2}$$

where the subscripts s, g and w refer to the solid, gas and water (or brine), respectively. The contact angle between gas-brine interfaces and the solid surface, and the gas-brine IFT are related to the capillary pressure via the Young-Laplace equation:

$$P_C = p_{nw} - p_w = \frac{2\gamma\cos(\theta)}{r} \tag{3}$$

where P_c is the capillary pressure, r is the effective pore radius corresponding to the largest pore, p_w is the pressure in the wetting phase saturating the seal rock, p_{nw} is the pressure in the non-wetting phase and γ is the gas-brine interfacial tension.

Equation (2) shows that the wettability of the mineral surface increases with rock-gas IFT and decreases with rock-water and water-gas IFTs. Equation (3) quantifies the pressure at which the non-wetting phase penetrates the largest pore of a caprock previously saturated with the wetting phase (brine or water). This pressure can be positive or negative, depending on the wettability of the rock [23,36]. As an example of the applicability of these equations, Hosseini et al. [37] showed quantitatively that increasing contact angles with temperature and pressure reduces the capillary sealing efficiency of shale rocks. The trend with pressure is related to the increase in contact angles, consistent with some of the studies summarized. Although the water wettability of shale samples studied increase at higher temperatures, the reduction in IFT was more significant, leading to an overall decrease in the capillary entry pressure.

Although the results just reviewed provide a generally consistent picture, some gaps remain, especially concerning the role of the nature of the rock surface and the rock-fluid interactions in determining the interfacial and wetting properties for systems relevant to underground hydrogen storage (UHS). Molecular simulations are well suited for

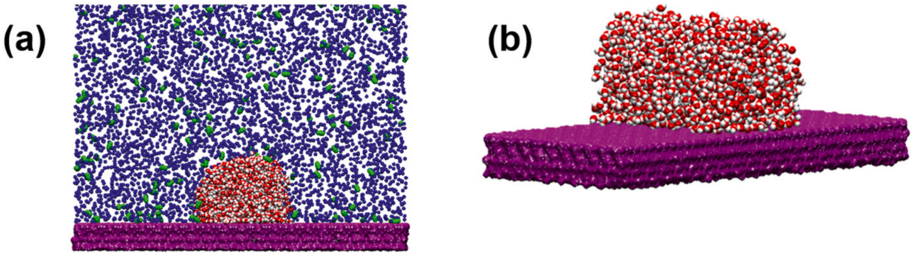

Fig. 1. Initial configuration of a water droplet on the siloxane surface of kaolinite. Kaolinite (siloxane) surface = purple; oxygen (water) = red; hydrogen (water) = white; hydrogen (gas) = blue and CO_2/CH_4 = green. (For interpretation of the references to colour in this figure legend, the reader is referred to the Web version of this article.)

addressing these knowledge gaps, as our group demonstrated for a few important interfacial systems [38–42].

To improve hydrogen recovery and reduce losses of hydrogen during withdrawal, UHS requires a cushion gas, such as CO_2, CH_4, and N_2, to maintain the reservoir pressure high as hydrogen is recovered from the reservoir. Kanaani et al. [43] found that N_2 and CH_4 increase both reservoir pressure and subsequent hydrogen recovery more effectively than CO_2. It has been suggested that cushion gases that yield higher gas wettability on a mineral surface, compared to H_2, promote easier separation during injection or withdrawal of hydrogen due to stronger interaction of the cushion gases with the surface [4]. It has also been suggested that density differences can be used as a criterion for selecting an appropriate cushion gas [44]. In Al-Yaseri et al.'s study of the wettability of clays, nitrogen, CO_2, helium and argon showed stronger gas-wetting behaviour on kaolinite, illite, and montmorillonite clays, suggesting their suitability as cushion gases [22]. This was in line with clay-H_2 IFT being higher than clay-N_2 and clay-CO_2 IFTs, as derived from experimental contact angles and gas-liquid IFT data using Neumann's equations of state [45]. Ali et al. [46] also observed higher contact angles and lower solid-gas IFTs for mica–CO_2–brine compared to mica-H_2-brine systems. Isfehani et al. [27] reported that the IFT of brine + H_2 + CO_2 reduces with increasing CO_2 concentrations. The density of mixed gas increases with the fraction of CO_2 which decreases the density difference between gas mixture and water solution, leading to IFT reductions.

Although there have also been experimental studies on methane as cushion gas [29,47,48], less extensive studies have been reported for the effect of H_2 on wettability of clays, as well as quantifying the effects of cushion gases on such features. To help fill this knowledge gap, we conducted molecular dynamics (MD) simulations to determine the effects of CO_2 and CH_4 on the contact angles of aqueous brine (10 wt% NaCl) on the kaolinite clay surface as a function of pressure. To complement our contact angle observations, we determined gas-liquid interfacial tensions at the conditions chosen for the wettability simulations. The results are interpreted towards identifying which gas is more effective for managing underground hydrogen storage.

The manuscript is organized as follows: Section 2 provides models and force fields details. In Section 3, the results in terms of contact angles and IFT are presented and discussed, where possible with the aid of experimental data from literature. Finally, conclusions are drawn.

2. Simulation details

2.1. Model setup

Kaolinite ($Al_2O_32SiO_2.2H_2O$), one of the most abundant clay minerals, is a 1:1 layered aluminosilicate with alternating sheets of silica (SiO_4) tetrahedral and octahedral alumina oxyhydroxides joined by apical oxygen atoms [49,50]. In our simulations, kaolinite was cleaved along the 001 or 00–1 basal plane, normal to the Z axis. The silica tetrahedron surface, often referred to as the siloxane surface, is hydrophobic. The alumina octahedral terminated with a plane of surface hydroxyl groups is the hydrophilic gibbsite surface. The kaolinite surface was placed parallel to the X–Y plane. The interactions between the two surfaces strongly depend on the relative orientation and on the presence of salt in the aqueous systems [51].

Table 1
Compositions of systems containing water droplets deposited on the siloxane surface of kaolinite simulated in this work.

System	Number of molecules			
H_2 – Cushion gas percentage by weight	Water	NaCl	H_2	Cushion gas (CO_2/CH_4)
100% H_2	2500	77	4500	0
50% H_2 – 50% CO_2	2500	77	4500	206
10% H_2 – 90% CO2	2500	77	4500	1841
100% CO_2	2500	77	0	14000
50% H_2 – 50% CH_4	2500	77	4500	563
10% H_2 – 90% CH_4	2500	77	4500	5065
100% CH_4	2500	77	0	5650

There were two sets of systems used for the determination of contact angles. In Fig. 1, we illustrate the setup for the first set of calculations, in which we placed a cylindrical water droplet containing 2500 water molecules and NaCl ions yielding 10 wt% NaCl on the kaolinite siloxane surface. The cylindrical droplet shape, infinitely long across the periodic boundaries, eliminates effects due to the three-phase contact line in the determination of the contact angle [51–53]. The droplet was surrounded by varying compositions of hydrogen (H_2), methane (CH_4), and carbon dioxide (CO_2), as shown in Table 1. The brine droplet was placed on the siloxane part of kaolinite because we observed complete spreading of water on the gibbsite surface, which also corroborates previous MD simulations [54]. To confirm the choice of the number of water molecules used to create the droplet, we performed a number of simulations with the water droplet containing 4000 water molecules. Our results (Table S1 in Supplementary Information – SI) showed that the contact angles did not increase significantly, while the simulations become more computationally expensive. A second set of calculations was carried out by placing one cylindrical gaseous bubble containing H_2, CO_2 and CH_4, on the hydrophilic part of the kaolinite surface and surrounding the bubble with 10 wt% NaCl brine. The number of molecules in these systems is presented in Table S2 of the Supporting Information.

The cylindrical droplets/bubbles were oriented parallel to the X direction, resulting in a solid-fluid interface perpendicular to the Z direction. The simulation box of size 51.98 × 179.64 × 200 A^3 was periodic in all three directions. The Y dimension of the simulation box was extended to prevent spurious effects due to interactions across the periodic boundary conditions, which were applied in the 3 directions.

To calculate brine – gas interfacial tensions (IFT), we placed 3000 water molecules at the centre of a simulation box, forming a liquid film of thickness ~ 45 Å parallel to the XY plane of the simulation box. Various numbers of H_2, CO_2, and CH_4 molecules were positioned on either side of the liquid film within the simulation box to represent the cushion gas composition being studied. The X, Y, and Z dimensions of

Table 2
Wettability classes based on gas - brine - kaolinite contact angles, as described by Ref. [[23]].

Contact Angle (°)							
	0	**0–50**	**50–70**	**70–110**	**110–130**	**130–180**	**180**
Wettability	Complete wetting	Strongly water – wet	Weakly water – wet	Intermediate – wet	Weakly Gas – wet	Strongly Gas – wet	Complete nonwetting

the box used for IFT calculations were 50, 50, and 100 Å, respectively. This set up has been applied previously in our group to produce realistic CO_2-water IFTs [55]. System compositions are shown in Table S3 of the SI. The approach implemented is similar to previous studies from our group [56].

2.2. Force fields

The kaolinite surfaces were modelled using the CLAYFF forcefield [57], following prior studies of wettability for kaolinite [54]. Water was represented by the rigid SPC/E [58] model and NaCl ions were modelled as charged Lennard-Jones (LJ) spheres using the Joung – Cheatham (JC) [59] force field without polarizability. The transferable potential for phase equilibria (TraPPE-UA) force field [60] was used to describe methane because it correctly describes the critical properties and vapor-liquid coexistence of linear alkanes far from the critical point. We used the flexible EPM2 model reported by Cygan et al. [61] for CO_2. This model improves the predictions of the interfacial and thermodynamic properties and correctly predicts the vibrational spectra of CO_2.

Two commonly used models were considered for simulating hydrogen. The single site Buch model [62] has the capability of reproducing the bulk thermodynamic properties of hydrogen up to high pressures (100 MPa). The 3-site Marx forcefield [63] also includes a quadrupole moment. Previous studies showed that both force fields predict density, viscosity, diffusion coefficients, and fugacity coefficient in good agreement with experiments up to 1000 bar [64,65]. To evaluate the suitability of both models for the purposes of this study, we conducted test simulations at 323K and 20 MPa to compare the simulated densities, contact angle, and interfacial tension against experimental data. The results are reported in Table S4 of the SI. We found that the contact angles and gas-liquid IFTs are comparable when either force field is implemented. The Buch model was selected because it yields a density of H_2 closer to the experimental 13.3 kgm^{-3}, and because it also reduces the computational costs compared to the 3-site Marx force field. Notably, the mutual solubilities of the gases (H_2, CO_2, and CH_4) simulated can be studied via the PC-SAFT equation of state (EOS). For completeness, we point out that our simulations yield densities for the gaseous systems that are in good agreement with experiments. The PC-SAFT also reproduces gas densities at a wide range of temperatures and pressures, as collated on the NIST dataset [66–71].

Dispersive forces were modelled by the 12–6 Lennard – Jones (LJ) potential, with the Lorentz-Berthelot mixing rules [72] applied to determine the LJ parameters for unlike interactions. Coulombic potentials were considered for describing electrostatic interactions. For all interatomic interactions, the cut-off distance for short range interactions was set to 12 Å, with long-range electrostatic interactions calculated using the particle mesh Ewald (PME) method [73].

2.3. Algorithms

The GROMACS package version 2018.2 [74] was utilized to perform equilibrium MD simulations. After energy minimization, the system was relaxed for 1 ns in the NVT ensemble. During these simulations, the kaolinite surface was kept rigid. Subsequently, NPT simulations were performed at 323 K and varying pressures between 5 and 40 MPa. The pressure was controlled by changing the Z dimension of the simulation box, perpendicular to the kaolinite surface. During the NPT simulations, we applied harmonic restraints on the kaolinite surface, with a force constant of 1000 kJ/mol nm [2]. The equations of motion were solved with the leap-frog algorithm [75] with a timestep of 1 fs. For the contact angle measurements, we conducted 35 ns equilibrium simulations followed by 5 ns production runs. Contact angles were calculated every 1 ns. Equilibrium was considered reached when the droplet shape did not change within 10 ns.

To evaluate the gas-liquid interfacial tensions, we conducted equilibration simulations for 20 ns followed by 10 ns production runs. The IFT was extracted via the anisotropy of the diagonal elements of the pressure tensor:

$$\gamma = \frac{1}{2} L_Z \left(P_{ZZ} - 0.5\left(P_{xx} + P_{yy}\right)\right) \tag{4}$$

where Lz is the length of the simulation box in the direction perpendicular to the gas/liquid interface. Pzz is the perpendicular component of the pressure tensor, Pxx, and Pyy are the tangential components of the pressure tensor.

This method for calculating interfacial tensions has been applied successfully in previous studies in our group [55,56,76–78]. Each IFT simulation was repeated three times to ensure reproducibility. To confirm equilibrium, we checked the system's energy and density profiles perpendicular to the gas-water interfaces, following prior efforts in the literature. The uncertainties in the calculations were estimated as one standard deviation among the mean of the results obtained.

The temperature of kaolinite and the fluids were controlled separately with two Berendsen thermostats, with a relaxation time of 100 fs. The Berendsen barostat was used to control the pressure [79]. Pressure coupling was applied only along the Z-direction, leaving the X and Y dimensions of the simulation box unchanged.

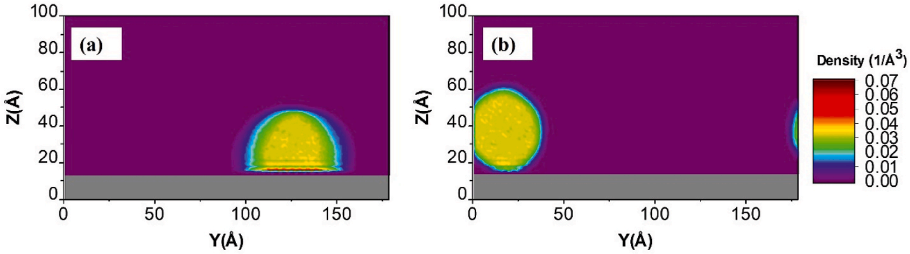

Fig. 2. 2D density distributions of water oxygen atoms for simulations conducted at 323 K and 20 MPa for systems(a) 100% H_2, and (b) 100% CO_2 environments, on the siloxane surface of kaolinite. The colour bar expresses density in the units of 1/Å^3. The grey rectangle illustrates the position of the siloxane kaolinite surface. (For interpretation of the references to colour in this figure legend, the reader is referred to the Web version of this article.)

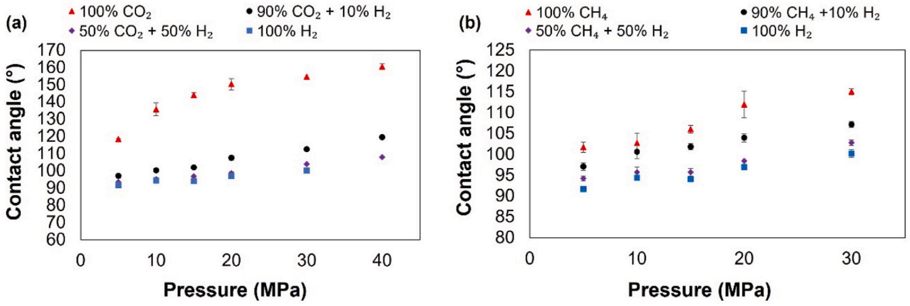

Fig. 3. Effects of (a) CO_2 gas-mixtures and (b) CH_4 gas-mixtures on the contact angles of a brine droplet on the siloxane surface of kaolinite, at 323 K and 5–40 MPa. These compositions are expressed as mass percentages. Error bars are expressed as one standard deviation from the mean values. Note that some of the errors calculated are smaller than the symbols.

3. Results and discussion

3.1. Siloxane surface

3.1.1. Contact angle

In Table 2, as a foundational basis to our discussion, we report the qualitative relationship between contact angle and wettability, which served as the basis for semi-quantitative analysis of our results.

The contact angle is estimated from 2D Y-Z surface density contours of the water molecules within the simulated droplets in the plane perpendicular to both the surface and the axis of symmetry of the cylindrical droplet. The 2D density profiles presented in Fig. 2 illustrate the transition of the droplet on the siloxane surface of kaolinite from hemicylindrical to nearly detached from the surface in the 100% CO_2 environment. The density contour for the 100% CO_2 environment aligns with the MD results from Tenney and Cygan [80] for a water droplet on a kaolinite siloxane surface at 330 K and 20 MPa. The hydrophobic nature of the surface causes the droplet to be mobile through the simulation box. This mobility was not quantified further.

Using 2D contours such as those in Fig. 2, the location of the droplet interface is defined as the density halfway between the density of water in the gas phase and that of bulk liquid water density at the centre of the droplet. A circular fit is then applied for each interface, with the slope of the tangent lines on both sides of the fit used to extract the contact angle, as illustrated in Fig. S1 of the SI. Because of density fluctuations near the surface, the density profiles within the first 10 Å from the surface were ignored. Similar methods have been used previously in our group [51, 55,81].

In Fig. 3 and Table S5 (SI), we present the brine contact angles on the siloxane surface of kaolinite as a function of pressure. In all systems, increasing pressure leads to higher contact angles, which is consistent with experimental results from literature [20–22]. In the experimental studies, the increase in contact angles with pressure was attributed to enhanced intermolecular interactions between the gases and the mineral surface, a consequence of the increase in molecular gas densities, which we also observed in our simulations.

In the case of pure CO_2 (panel a), the contact angles range from ~118° at 5 MPa to ~160° at 40 MPa, indicating a change in the surface wettability from weakly 'gas-wet' towards strongly 'gas-wet'. This can be attributed to relatively strong interactions between CO_2 and the siloxane surface. The simulated contact angles compare well with those obtained experimentally on hydrophobic polytetrafluoroethylene (PTFE) and oil-wet mica [82,83].

The replacement of 10 wt% CO_2 with hydrogen leads to significant reductions in the contact angles, suggesting that a small amount of hydrogen increases the hydrophilicity of the siloxane surface. For example, at 20 MPa, the brine contact angle in pure CO_2 is 154° and in the 90 wt% CO_2 system, the contact angle drops to 106°. Further increase in H_2 content has no salient effects on wettability. In systems with only H_2, the contact angle ranges from 91° to 106° as pressure changes, showing that the surface stays 'intermediate wet' within the conditions studied, thus pressure has no significant effect on the wettability for pure H_2 systems. This suggests that the changes in the hydrogen gas density in the pressure range considered are not enough to cause a significant increase in contact angles. Consistent with our observations, several experiments have reported slight pressure effects on contact angles in the presence of H_2 [11–13].

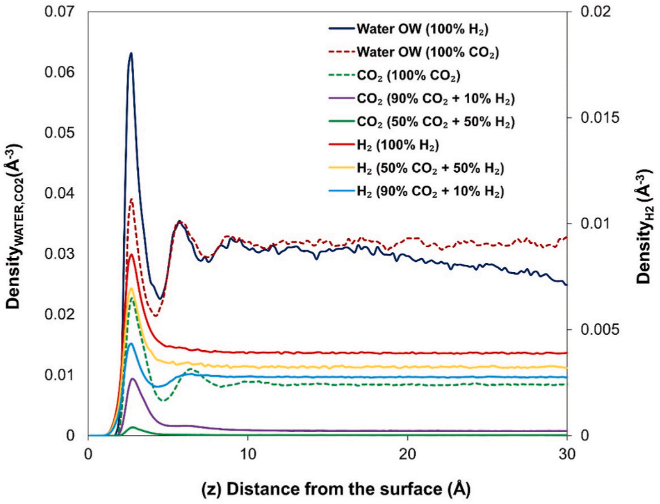

Fig. 4. Atomic density profiles along the Z direction, normal to the surface, for oxygen atoms of water, carbon atoms of CO_2, and H_2 at 323 K and 20 MPa. Note that a single-site model was implemented to simulate H_2. Compositions stated are mass percentages. The reference ($Z = 0$) corresponds to the plane formed by the topmost oxygen atoms on the silica tetrahedra at the top of the siloxane surface of kaolinite.

As evident in Fig. 3, panel b, the effects of methane on wettability are less pronounced than those due to CO_2, although the same trend of increasing contact angles with pressure is observed. At all pressures, the increase in contact angles between the systems with only H_2 and only CH_4 does not exceed 15°. Similarly, Alanazi et al. [48] showed small effects of CH_4 on shale rocks, for pure gases (H_2 or CH_4) and 50:50 CH_4:H_2 mixtures. Furthermore, oil-wet sandstone and limestone surfaces remained weakly water-wet in the presence of methane, at ~6.9 MPa and 22–60 °C [29].

Recent experiments on clays showed that in the presence of H_2, contact angles for 20 wt% NaCl brines remained <40° at pressures up to 20 MPa [22]. The discrepancy with our results could be attributed to the two basal planes of kaolinite. In the present study, the hydrophobic siloxane surface (00–1 plane) of kaolinite was used, while it is possible that the hydrophilic gibbsite surface (001) was more dominant in the experiment reported by Al-Yaseri et al. [22].

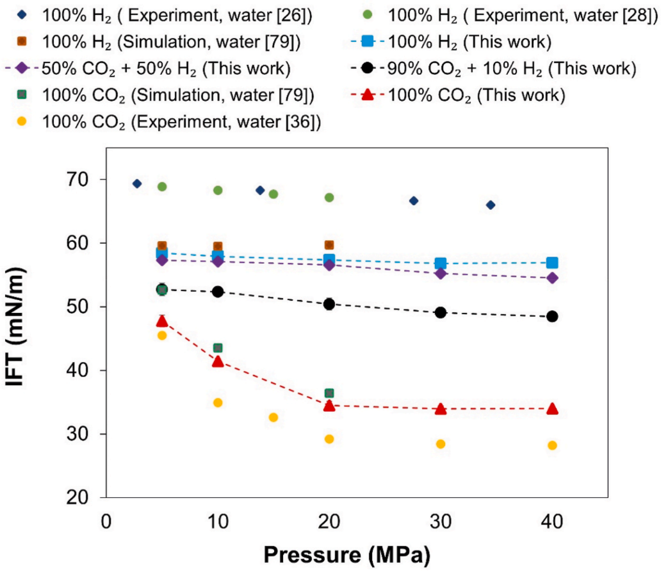

Fig. 5. Interfacial tension (IFT) of CO_2/H_2/brine systems as a function of pressure at 323 K. These compositions are expressed as mass percentages. Error bars are expressed as one standard deviation from the mean. Note that some of the error bars calculated are smaller than the symbols.

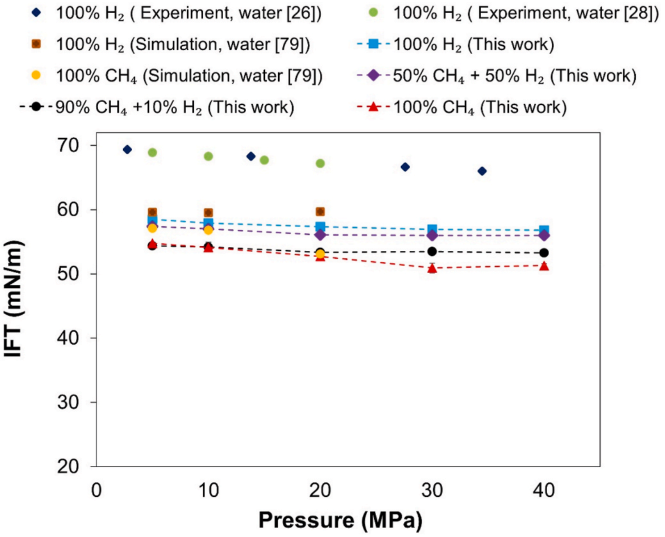

Fig. 6. Interfacial tension (IFT) of CH_4/H_2/brine systems as a function of pressure at 323 K. The compositions of the systems investigated are expressed as mass percentages. Error bars are expressed as one standard deviation from the mean. Note that some of the error bars are smaller than the symbols.

To investigate the solid-fluid interactions further, we computed the atomic density distributions of the water droplet by monitoring the position of the oxygen atoms (OW) along the axis passing through the centre of the droplet. The positions of CO_2 (monitoring the position of the carbon atoms), CH_4, and H_2, outside the water droplet, as a function of the distance Z normal from the siloxane surface are also monitored in our analysis. Note that CH_4 and H_2 are treated as united atom molecules in our simulations, hence they are defined by the position of their center, rather than via the position of the atomic constituents. The plane of the topmost oxygen atoms on the silica tetrahedral layer at the top of the siloxane surface was used as the reference point ($Z = 0$). For clarity, because the structure of the water droplet near the surface is similar in all systems (see Fig. S2 in SI), only the profiles in 100% CO_2, 100% CH_4 and 100% H_2 are shown. The results are shown in Fig. 4. The water molecules within the droplet form two distinct hydration layers near the surface. The first peak is located at ~2.7 Å from the surface while the second appears at ~5.7 Å. Interestingly, the first peaks corresponding to CO_2 and H_2 are found within the first hydration layer observed for the brines. However, their densities are much lower, as they are gases at the conditions simulated. Comparison of results obtained for CO_2 and H_2 shows that adding CO_2 to the system reduces the density of H_2 molecules adsorbed near the surface, although the amount of H_2 in the system is constant. It is noted that CO_2 also displaces some water molecules from the surface. It appears that the substantial reduction observed in the contact angles can be attributed to the stronger interactions between CO_2 and the surface, compared to the H_2-surface interactions. These results highlight the importance of gases adsorbing at the solid-liquid and solid-gas interfaces in determining contact angles. These effects are expected to strongly depend on fluid composition, surface features, as well as system temperature and pressure. Trends similar to those just discussed are documented for systems with CH_4 as well (Fig. S3 in SI). The main difference observed is that the first peak corresponding to CH_4 appears at ~3.1 Å whereas H_2 is still found within the first hydration layer at ~2.7 Å.

3.1.2. *Gas – brine interfacial tension (IFT)*

In Figs. 5 and 6, we present the effects of the gas mixture compositions on gas – brine IFTs. The data are tabulated in Table S6 of SI. IFT decreased with pressure, however, the extent of the decrease is more pronounced in the systems with higher percentage of CO_2 or CH_4. For example, increasing the pressure from 5 to 40 MPa changes the pure H_2/brine IFT by 2 mN/m, whereas the IFT change in pure CO_2/brine and pure CH_4/brine are 15 mN/m and 4 mN/m, respectively (Fig. 5). Because hydrogen has a lower density, it is possible that a very significant increase in pressure is required to cause significant changes in IFT. The minimum pressure used in our simulations was 5 MPa, therefore it is not possible to validate the increase in H_2-water IFT observed by Chow et al. [28] at pressures below 5 MPa. Between 5 and 20 MPa, the CO_2/brine IFTs decrease almost linearly with pressure, until the IFT approaches a plateau of ~34.1 mN/m. Bachu and Bennion reported comparable findings in their experimental measurements of CO_2-brine IFTs [84]. Chiquet et al. [36] also found that at temperature conditions similar to those considered here, the IFT becomes relatively constant above 20 MPa.

The IFTs for the gas mixtures are found to be in between the values obtained for the pure gases, with the results corresponding to 50 wt% H_2 being nearly the same as 100% H_2 for both CO_2 and CH_4 systems. In systems with CH_4 (Fig. 6), the IFT results for systems with 10 wt% H_2 almost overlap with pure CH_4/brine IFTs, at pressures up to 20 MPa. The increase in methane vs. hydrogen content reduces the IFT slightly. For systems with CH_4, the IFT changed from 57.3 mN/m, for 100% H_2 systems, to 52.7 mN/m for 100% CH_4. We found that the presence of 10% H_2 also leads to a significant increase in IFT in systems with CO_2. These IFT results could be attributed to interactions between brine and the CO_2/CH_4 molecules at the interface compared to brine-H_2 interactions. The results are consistent with other simulation results [85]. Comparison to experimental data also shows similar trends in IFT with pressure [26,28,36].

There have been several methods developed to describe interfaces in simulations. Berkowitz et al., e.g., [86] developed an algorithm for computing density profiles at rough liquid - gas/solid interfaces. In our systems, interfacial molecules are identified by implementing the algorithm proposed by Willard and Chandler [87], where the interface is identified as the point the coarse-grained density is half the density of bulk water. The density profiles in the Z direction, normal to the gas-liquid interface, are provided in Figs. 7 and 8. As cushion gases are added to the systems, gas accumulates at the interface compared to pure H_2 systems. This results in enhanced interfacial activities in systems containing CH_4 and CO_2, lowering the IFT.

The gas-brine IFT results obtained in our simulations were found to

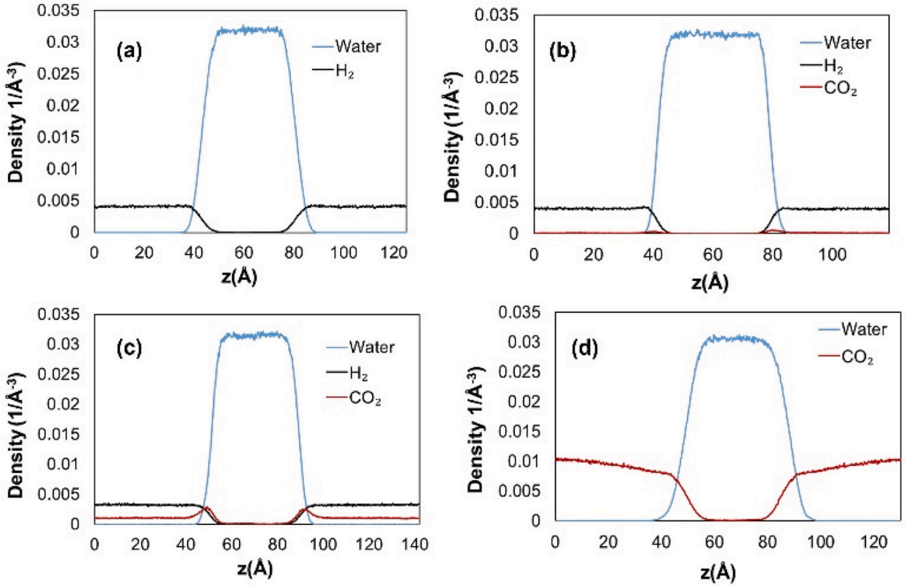

Fig. 7. Density profiles in the Z direction, normal to the liquid-gas interface, for (a) 100% H_2/Brine, (b) 50%H_2+50%CO_2/Brine, (c) 10%H_2+90%CO_2/Brine and (d) 100% CO_2/Brine systems. The simulations were conducted at T = 323 K and P = 20 MPa. The composition percentages are calculated based on mass.

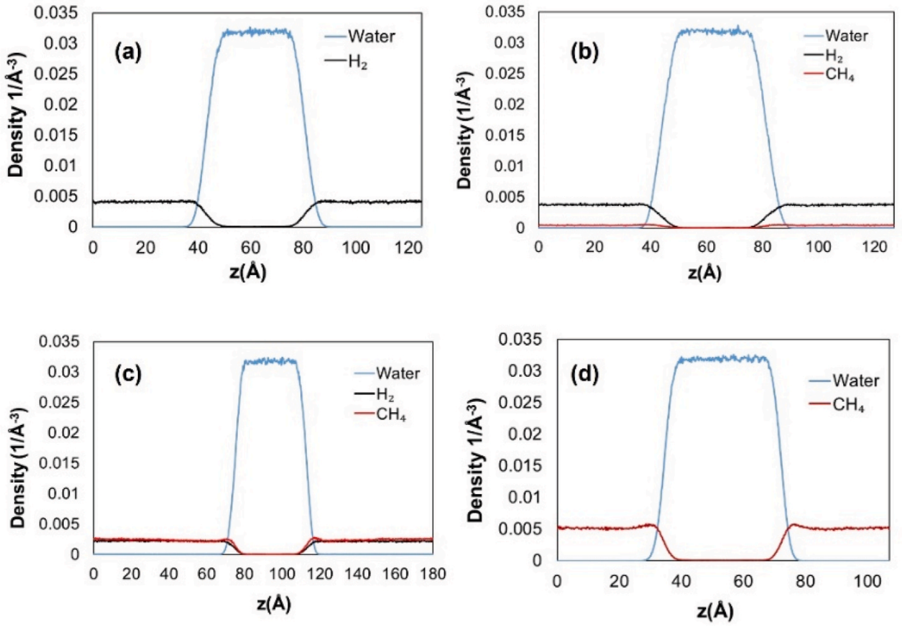

Fig. 8. Density profiles along the Z direction, normal to the gas-liquid interface, for (a) 100% H_2/Brine, (b) 50% H_2+50%CH_4/Brine, (c) 10%H_2+90%CH_4/Brine and (d) 100% CH_4/Brine systems. The simulations were conducted at T = 323 K and P = 20 MPa. The composition percentages are by mass.

Table 3

Difference in densities observed between the H_2O-rich phase and the gas-rich phase, for IFT simulations conducted at 323 K and 20 MPa. The composition percentages are by mass.

System composition	CO_2 systems (kgm^{-3})	CH_4 systems (kgm^{-3})
100% H_2	939.6	939.6
50% H_2	927.7	928.1
10% H_2	852.6	875.5
0% H_2	192.1	815.7

scale with the density difference between liquid and gas phases. This means that a reduction in the density difference should lead to a reduction in IFT. In Table 3, we report the difference in density observed between the brine phase and the gas phases. The difference in density correlates with slight reduction in IFT for systems contacting CO_2, compared with CH_4, which corroborates our results thus far. This reduction in density difference is responsible for the increase in adhesive forces between the gases and brine at the interface, which reduces the IFT. CH_4 has a lower density than CO_2, therefore its effect is weaker on IFT changes with pressure. Although a reduction in gas-brine IFT should increase the water wettability of the surface (based on Equation (2)), the surface becomes more gas-wet when CO_2 or CH_4 is added. This correlates with the IFT between the gas and the surface decreasing in the

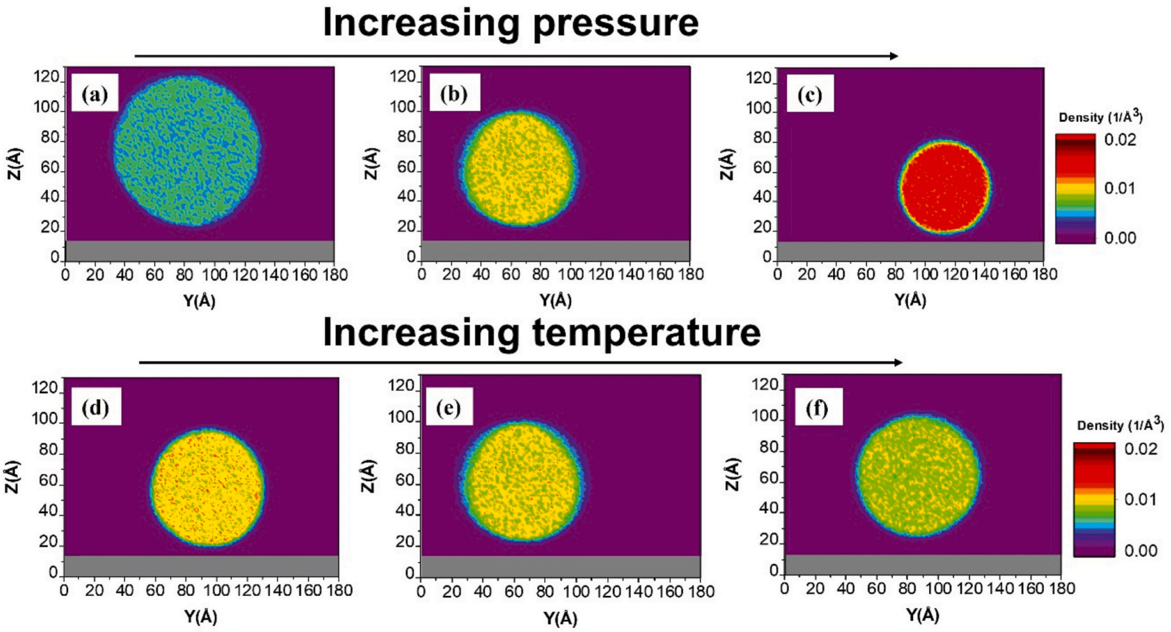

Fig. 9. 2D density profiles of the H_2 bubble near the gibbsite surface of kaolinite. The simulations were conducted at (a) 323 K & 20 MPa (b) 323 K & 40 MPa (c) 323 K & 80 MPa (d) 303 K & 40 MPa (e) 323 K & 40 MPa, and (f) 343 K & 40 MPa. The colour bar expresses density in the units of 1/Å^3. (For interpretation of the references to colour in this figure legend, the reader is referred to the Web version of this article.)

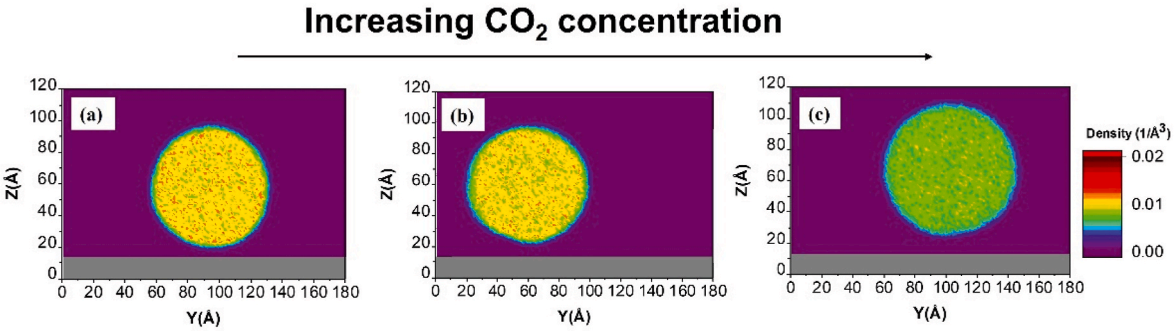

Fig. 10. 2D density profiles of the H_2 bubble on the gibbsite surface of kaolinite. The simulations were conducted with (a) 100% H_2 (b) 50% H_2 & 50% CO_2 and (c) 10% H_2 & 90% CO_2 at 303 K & 40 MPa. The percentages are by mass. The colour bar expresses density in the units of 1/Å^3. (For interpretation of the references to colour in this figure legend, the reader is referred to the Web version of this article.)

presence of the cushion gases.

3.2. Gibbsite surface

3.2.1. Hydrogen bubbles on the gibbsite surface of kaolinite

To complement the results for brine contact angles on the siloxane (hydrophobic) surface, we placed hydrogen gas as cylindrical bubbles near the gibbsite (hydrophilic) surface of kaolinite. We studied the effects of pressure (20–80 MPa) and temperature (30–70 °C), as shown in Fig. 9. In all systems, hydrogen forms a cylindrical droplet detached from the surface, indicative of the strong water wettability of the surface. Increasing the pressure from 20 to 80 MPa at 323 K (Fig. 9 panels a–c), produces a denser, more compact hydrogen bubble. The circular fit around the bubble was estimated by applying a similar algorithm to the one used to characterize the water droplets. The radius of this circular fit reduced from ~50.5 Å at 20 MPa to ~33.0 Å at 80 MPa, which is consistent with the increase in water contact angles in the same pressure range. The effects of temperature are less noticeable; nonetheless, in Fig. 9 panels d–f, we observe a reduction in the affinity between the hydrogen bubble and the surface at high temperature. This is consistent with the increase in water wettability with temperature reported for mica [20], but not with the reduction in wettability observed for quartz [21]. Although the hydroxyl ions on the gibbsite surface can form hydrogen bonds with water, it seems that the reduction in H_2 density at higher temperatures contributes more significantly to the observed trend. The results were confirmed by conducting simulations with varying concentrations of CO_2 added to the hydrogen droplet. The 2-D density profiles presented in Fig. 10 corroborate the reduction in H_2 density at the surface observed as the concentration of CO_2 increases. These results show that water droplets on both the hydrophobic and hydrophilic parts of kaolinite respond to changes in pressure and temperature in similar manners.

4. Conclusions

Molecular dynamics simulations were conducted to investigate physical, chemical, and interfacial properties important for the possible use of CO_2 and CH_4 as cushion gases during underground hydrogen storage. The model rock interface was kaolinite, an abundant clay mineral often found in geological repositories, chosen because of its importance in the energy sector. Calculations of contact angles on the siloxane surface of kaolinite and brine – gas interfacial tension were carried out while varying the concentration of CO_2 or CH_4 at 323 K and at pressures up to 40 MPa. At all pressures, the presence of both cushion gases increased the contact angles of NaCl brines on the surface due to stronger interactions of the gases with the siloxane kaolinite surface, although CO_2 exhibited a stronger effect. Our results also documented a reduction in the brine – gas interfacial tension as the concentration of cushion gases increases, because of the decrease in the difference between liquid and gas densities. Because higher contact angles and lower gas-brine IFTs reduce the capillary sealing pressure, both CO_2 and CH_4 reduce the pressure required to displace brine from the mineral pores. This in turn reduces the trapping capacity of hydrogen. Conversely, these effects are likely to increase the recovery of hydrogen during withdrawal.

To identify the molecular mechanisms responsible for the observed results, we investigated preferential adsorption of various molecules in contact with the solid substrate. For example, the planar density profiles for hydrogen droplets on the hydrophilic gibbsite surface showed that lower pressures and higher temperatures reduce the affinity between hydrogen and the mineral surface, suggesting that wettability increases at these conditions. This corroborates the results obtained on the hydrophobic siloxane surface. Although there is a reduction in the H_2 density at the surface in the presence of CO_2, the increase in CO_2 density leads to an overall lower surface wettability.

Ultimately, interfacial tensions and contact angles determine the sealing pressure in the reservoir. We expect that intermediate to weakly – gas wetting could be favourable for this application. Because the cushion gases have stronger interactions with the surface (shown by the contact angle results), their presence is expected to increase the recovery of hydrogen. One optimum strategy could consider adding a small fraction of gases with densities between hydrogen and water, which contribute to successful intermittent storage of hydrogen, although this possibility needs to be tested.

Declaration of competing interest

The Authors declare no conflict of interest.

Acknowledgements

The Authors acknowledge the financial support from the U.S. Department of Energy, Office of Basic Energy Sciences, under Contract No. DE-SC0006878 (Division of Chemical Sciences, Geosciences, and Biosciences), Geosciences Program. AA was supported by the UK EPSRC Centre for Doctoral Training in the Advanced Characterisation of Materials (Grant No. EP/S023259/1). We are grateful to the University College London Research Computing Platforms Support (MYRAID and KATHLEEN) and the UK Materials, and Molecular Modelling Hub (YOUNG) for access to high-performance computing. AS acknowledges support from the Asahi Glass Chair of Chemical Engineering at the University of Oklahoma, as well as from the US National Science Foundation under grant number 2317726.

Appendix A. Supplementary data

Supplementary data to this article can be found online at https://doi.org/10.1016/j.ijhydene.2024.01.151.

References

[1] Shiva Kumar S, Lim H. An overview of water electrolysis technologies for green hydrogen production. Energy Rep 2022;8:13793–813.

[2] Gov Energy. Hydrogen storage. Available from: https://www.energy.gov/eere/fuelcells/hydrogen-storage; 2023.

[3] Gabrielli P, Poluzzi A, Kramer GJ, Spiers C, Mazzotti M, Gazzani M. Seasonal energy storage for Zero-Emissions multi-energy systems via underground hydrogen torage. Renewable Sustainable Energy Rev 2020;121:109629.

[4] Muhammed NS, Haq B, Al Shehri D, Al-Ahmed A, Rahman MM, Zaman E. A review on underground hydrogen storage: insight into geological sites, influencing factors and future outlook. Energy Rep 2022;8:461–99.

[5] Phan A, Cole DR, Weiß RG, Dzubiella J, Striolo A. Confined water determines transport properties of guest molecules in narrow pores. ACS Nano 2016;10:7646–56.

[6] Marmur A. Solid-surface characterization by wetting. Annu Rev Mater Res 2009;39:473–89.

[7] Abraham M, Claudio DV, Stefano S, Alidad A, D. J W. Contact angles and wettability: towards common and accurate terminology. Surf Innovations 2017;5:3–8.

[8] Sedev R, Akhondzadeh H, Ali M, Keshavarz A, Iglauer S. Contact angles of a brine on a bituminous coal in compressed hydrogen. Geophys Res Lett 2022;49:e2022GL098261.

[9] Hosseini M, Ali M, Fahimpour J, Keshavarz A, Iglauer S. Basalt-H2-brine wettability at geo-storage conditions: implication for hydrogen storage in basaltic formations. J Energy Storage 2022;52:104745.

[10] Hou J, Lin S, Zhang M, Li W. Salinity, temperature and pressure effect on hydrogen wettability of carbonate rocks. Int J Hydrogen Energy 2023;48:11303–11.

[11] Al-Yaseri A, Abu-Mahfouz IS, Yekeen N, Wolff-Boenisch D. Organic-rich source rock/H2/brine interactions: implications for underground hydrogen storage and methane production. J Energy Storage 2023;63:106986.

[12] Higgs S, Da Wang Y, Sun C, Ennis-King J, Jackson SJ, Armstrong RT, Mostaghimi P. In-situ hydrogen wettability characterisation for underground hydrogen storage. Int J Hydrogen Energy 2022;47:13062–75.

[13] Al-Mukainah H, Al-Yaseri A, Yekeen N, Hamad JA, Mahmoud M. Wettability of shale–brine–H2 system and H2-brine interfacial tension for assessment of the sealing capacities of shale formations during underground hydrogen storage. Energy Rep 2022;8:8830–43.

[14] Al-Yaseri A, Yekeen N, Mahmoud M, Kakati A, Xie Q, Giwelli A. Thermodynamic characterization of H2-brine-shale wettability: implications for hydrogen storage at subsurface. Int J Hydrogen Energy 2022;47:22510–21.

[15] Ali M, Yekeen N, Pal N, Keshavarz A, Iglauer S, Hoteit H. Influence of organic molecules on wetting characteristics of mica/H2/brine systems: implications for hydrogen structural trapping capacities. J Colloid Interface Sci 2022;608:1739–49.

[16] Zeng L, Hosseini M, Keshavarz A, Iglauer S, Lu Y, Xie Q. Hydrogen wettability in carbonate reservoirs: implication for underground hydrogen storage from geochemical perspective. Int J Hydrogen Energy 2022;47:25357–66.

[17] Iglauer S, Ali M, Keshavarz A. Hydrogen wettability of sandstone reservoirs: implications for hydrogen geo-storage. Geophys Res Lett 2021;48:e2020GL090814.

[18] Hosseini M, Fahimpour J, Ali M, Keshavarz A, Iglauer S. Hydrogen wettability of carbonate formations: implications for hydrogen geo-storage. J Colloid Interface Sci 2022;614:256–66.

[19] Hashemi L, Glerum W, Farajzadeh R, Hajibeygi H. Contact angle measurement forHydrogen/brine/sandstone system using captive-bubble method relevant for underground hydrogen storage. Adv Water Resour 2021;154:103964.

[20] Ali M, Yekeen N, Pal N, Keshavarz A, Iglauer S, Hoteit H. Influence of pressure, temperature and organic surface concentration on hydrogen wettability of caprock; implications for hydrogen geo-storage. Energy Rep 2021;7:5988–96.

[21] Ali M, Jha NK, Al-Yaseri A, Zhang Y, Iglauer S, Sarmadivaleh M. Hydrogen wettability of quartz substrates exposed to organic acids; Implications for hydrogen geo-storage in sandstone reservoirs. J Petrol Sci Eng 2021;207:109081.

[22] Al-Yaseri A, Wolff-Boenisch D, Fauziah CA, Iglauer S. Hydrogen wettability of clays: implications for underground hydrogen storage. Int J Hydrogen Energy 2021;46:34356–61.

[23] Iglauer S, Pentland CH, Busch A. CO2 wettability of seal and reservoir rocks and the implications for carbon geo-sequestration. Water Resour Res 2015;51:729–74.

[24] Zivar D, Kumar S, Foroozesh J. Underground hydrogen storage: a comprehensive review. Int J Hydrogen Energy 2021;46:23436–62.

[25] Georgiadis A, Maitland G, Trusler JPM, Bismarck A. Interfacial tension measurements of the (H2O + CO2) system at elevated pressures and temperatures. J Chem Eng Data 2010;55:4168–75.

[26] Hosseini M, Fahimpour J, Ali M, Keshavarz A, Iglauer S. H2−brine interfacial tension as a function of salinity, temperature, and pressure; implications for hydrogen geo-storage. J Petrol Sci Eng 2022;213:110441.

[27] Dalal Isfehani Z, Sheidaie A, Hosseini M, Fahimpour J, Iglauer S, Keshavarz A. Interfacial tensions of (brine + H2 + CO2) systems at gas geo-storage conditions. J Mol Liq 2023;374:121279.

[28] Chow YTF, Maitland GC, Trusler JPM. Interfacial tensions of (H2O + H2) and (H2O + CO2 + H2) systems at temperatures of (298–448) K and pressures up to 45 MPa. Fluid Phase Equil 2018;475:37–44.

[29] Mirchi V, Dejam M, Alvarado V. Interfacial tension and contact angle measurements for hydrogen-methane mixtures/brine/oil-wet rocks at reservoir conditions. Int J Hydrogen Energy 2022;47:34963–75.

[30] Omrani S, Ghasemi M, Singh M, Mahmoodpour S, Zhou T, Babaei M, Niasar V. Interfacial tension–temperature–pressure–salinity relationship for the hydrogen–brine system under reservoir conditions: integration of molecular dynamics and machine learning. Langmuir 2023;39:12680–91.

[31] Hosseini M, Ali M, Fahimpour J, Keshavarz A, Iglauer S. Assessment of rock-hydrogen and rock-water interfacial tension in shale, evaporite and basaltic rocks. J Nat Gas Sci Eng 2022;106:104743.

[32] Hosseini M, Ali M, Fahimpour J, Keshavarz A, Iglauer S. Calcite–fluid interfacial tension: H2 and CO2 geological storage in carbonates. Energy Fuel 2023;37:5986–94.

[33] Arif M, Barifcani A, Iglauer S. Solid/CO2 and solid/water interfacial tensions as a function of pressure, temperature, salinity and mineral type: implications for CO2-wettability and CO2 geo-storage. Int J Greenh Gas Control 2016;53:263–73.
[34] Esfandyari H, Hosseini M, Ali M, Iglauer S, Haghighi M, Keshavarz A. Assessment of the interfacial properties of various mineral/hydrogen/water systems. J Energy Storage 2023;60:106637.
[35] Young III T. An essay on the cohesion of fluids. Phil Trans Roy Soc Lond 1997;95:65–87.
[36] Chiquet P, Daridon J-L, Broseta D, Thibeau S. CO2/water interfacial tensions under pressure and temperature conditions of CO2 geological storage. Energy Convers Manag 2007;48:736–44.
[37] Hosseini M, Fahimpour J, Ali M, Keshavarz A, Iglauer S. Capillary sealing efficiency analysis of caprocks: implication for hydrogen geological storage. Energy Fuel 2022;36:4065–75.
[38] Phan A, Striolo A. Evidence of facilitated transport in crowded nanopores. J Phys Chem Lett 2020;11:1814–21.
[39] Striolo A, Huang S. Upcoming transformations in integrated energy/chemicals sectors: some challenges and several opportunities. J Phys Chem C 2022;126:21527–41.
[40] Striolo A. Clathrate hydrates: recent advances on CH4 and CO2 hydrates, and possible new frontiers. Mol Phys 2019;117:3556–68.
[41] Striolo A. Studying surfactants adsorption on heterogeneous substrates. Current Opinion in Chemical Engineering 2019;23:115–22.
[42] Striolo A, Michaelides A, Joly L. The carbon-water interface: modeling challenges and opportunities for the water-energy nexus. Annu Rev Chem Biomol Eng 2016;7:533–56.
[43] Kanaani M, Sedaee B, Asadian-Pakfar M. Role of cushion gas on underground hydrogen storage in depleted oil reservoirs. J Energy Storage 2022;45:103783.
[44] Feldmann F, Hagemann B, Ganzer L, Panfilov M. Numerical simulation of hydrodynamic and gas mixing processes in underground hydrogen storages. Environ Earth Sci 2016;75:1165.
[45] Yekeen N, Al-Yaseri A, Negash BM, Ali M, Giwelli A, Esteban L, Sarout J. Clay-hydrogen and clay-cushion gas interfacial tensions: implications for hydrogen storage. Int J Hydrogen Energy 2022;47:19155–67.
[46] Ali M, Pan B, Yekeen N, Al-Anssari S, Al-Anazi A, Keshavarz A, Iglauer S, Hoteit H. Assessment of wettability and rock-fluid interfacial tension of caprock: implications for hydrogen and carbon dioxide geo-storage. Int J Hydrogen Energy 2022;47:14104–20.
[47] Hashemi L, Boon M, Glerum W, Farajzadeh R, Hajibeygi H. A comparative study for H2–CH4 mixture wettability in sandstone porous rocks relevant to underground hydrogen storage. Adv Water Resour 2022;163:104165.
[48] Alanazi A, Yekeen N, Ali M, Ali M, Abu-Mahfouz IS, Keshavarz A, Iglauer S, Hoteit H. Influence of organics and gas mixing on hydrogen/brine and methane/brine wettability using Jordanian oil shale rocks: implications for hydrogen geological storage. J Energy Storage 2023;62:106865.
[49] Frost RL, Kristof J. Raman and infrared spectroscopic studies of kaolinite surfaces modified by intercalation. In: Wypych F, Satyanarayana KG, editors. Interface science and technology, vol. 1. Elsevier; 2004. p. 184–215.
[50] Bougeard D, Smirnov KS, Geidel E. Vibrational spectra and structure of kaolinite: a computer simulation study. J Phys Chem B 2000;104:9210–7.
[51] Le TTB, Striolo A, Cole DR. Supercritical CO2 effects on calcite wettability: a molecular perspective. J Phys Chem C 2020;124:18532–43.
[52] Rafiee J, Mi X, Gullapalli H, Thomas AV, Yavari F, Shi Y, Ajayan PM, Koratkar NA. Wetting transparency of graphene. Nat Mater 2012;11:217–22.
[53] Vanzo D, Bratko D, Luzar A. Wettability of pristine and alkyl-functionalized graphane. J Chem Phys 2012;137.
[54] Solc R, Gerzabek MH, Lischka H, Tunega D. Wettability of kaolinite (001) surfaces — molecular dynamic study. Geoderma 2011;169:47–54.
[55] Thi Bao Le T, Divine-Ayela C, Striolo A, Cole DR. Effects of surface contamination on the interfacial properties of CO2/water/calcite systems. Phys Chem Chem Phys 2021;23:18885–92.
[56] Phan A, Stamatakis M, Koh CA, Striolo A. Microscopic insights on clathrate hydrate growth from non-equilibrium molecular dynamics simulations. J Colloid Interface Sci 2023;649:185–93.
[57] Cygan RT, Liang J-J, Kalinichev AG. Molecular Models of Hydroxide, Oxyhydroxide, and clay phases and the development of a general force field. J Phys Chem B 2004;108:1255–66.
[58] Berendsen HJC, Grigera JR, Straatsma TP. The missing term in effective pair potentials. J Phys Chem 1987;91:6269–71.
[59] Joung IS, Cheatham TE. Determination of alkali and halide monovalent ion parameters for use in explicitly solvated biomolecular simulations. J Phys Chem B 2008;112:9020–41.
[60] Martin MG, Siepmann JI. Transferable potentials for phase equilibria. 1. United-atom description of n-alkanes. J Phys Chem B 1998;102:2569–77.
[61] Cygan RT, Romanov VN, Myshakin EM. Molecular simulation of carbon dioxide capture by montmorillonite using an accurate and flexible force field. J Phys Chem C 2012;116:13079–91.
[62] Buch V. Path integral simulations of mixed para-D2 and ortho-D2 clusters: the orientational effects. J Chem Phys 1994;100:7610–29.
[63] Marx D, Nielaba P. Path-integral Monte Carlo techniques for rotational motion in two dimensions: quenched, annealed, and no-spin quantum-statistical averages. Phys Rev 1992;45:8968–71.
[64] Rahbari A, Brenkman J, Hens R, Ramdin M, van den Broeke LJP, Schoon R, Henkes R, Moultos OA, Vlugt TJH. Solubility of water in hydrogen at high pressures: a molecular simulation study. J Chem Eng Data 2019;64:4103–15.
[65] Tsimpanogiannis IN, Maity S, Celebi AT, Moultos OA. Engineering model for predicting the intradiffusion coefficients of hydrogen and oxygen in vapor, liquid, and supercritical water based on molecular dynamics simulations. J Chem Eng Data 2021;66:3226–44.
[66] Eller J, Sauerborn T, Becker B, Buntic I, Gross J, Helmig R. Modeling subsurface hydrogen storage with transport properties from entropy scaling using the PC-saft equation of state. Water Resour Res 2022;58:e2021WR030885.
[67] Gonçalves AF, Castier M, Franco LFM. The role of cross-association between carbon dioxide and hydrogen sulfide using the SAFT-VR mie equation of state. Fluid Phase Equil 2022;559:113493.
[68] Alanazi A, Ali M, Bawazeer S, Yekeen N, Hoteit H. Evaluation of cubic, PC-SAFT, and GERG2008 equations of state for accurate calculations of thermophysical properties of hydrogen-blend mixtures. Energy Rep 2022;8:13876–99.
[69] Keller A, Langenbach K, Hasse H. Comparison of predictions of the PC-SAFT equation of state and molecular simulations for the metastable region of binary mixtures. Fluid Phase Equil 2017;444:31–6.
[70] Diamantonis NI, Boulougouris GC, Mansoor E, Tsangaris DM, Economou IG. Evaluation of cubic, SAFT, and PC-SAFT equations of state for the vapor–liquid equilibrium modeling of CO2 mixtures with other gases. Ind Eng Chem Res 2013;52:3933–42.
[71] Shi J, Li H. Modified temperature-dependent volume translation model in PC-SAFT equation of state for carbon dioxide. Chem Eng Sci 2022;263:118107.
[72] Allen MP, Tildesley D. J. *Computer Simulation of liquids*. Oxford, UK: Oxford University Press; 2004.
[73] Darden T, York DM, Pedersen LG. Particle mesh Ewald: an N·log(N) method for Ewald sums in large systems. J Chem Phys 1993;98:10089.
[74] Hess B, Kutzner C, van der Spoel D, Lindahl E. Gromacs 4: algorithms for highly efficient, load-balanced, and scalable molecular simulation. J Chem Theor Comput 2008;4:435–47.
[75] Mazur AK. Common molecular dynamics algorithms revisited: accuracy and optimal time steps of störmer–leapfrog integrators. J Comput Phys 1997;136:354–65.
[76] Badmos SB, Striolo A, Cole DR. Aqueous hydrogen sulfide in slit-shaped silica nanopores: confinement effects on solubility, structural, and dynamical properties. J Phys Chem C 2018;122:14744–55.
[77] Phan A, Stoner HM, Stamatakis M, Koh CA, Striolo A. Surface morphology effects on clathrate hydrate wettability. J Colloid Interface Sci 2022;611:421–31.
[78] Bui T, Frampton H, Huang S, Collins IR, Striolo A, Michaelides A. Water/oil interfacial tension reduction – an interfacial entropy driven process. Phys Chem Chem Phys 2021;23:25075–85.
[79] Berendsen HJC, Postma JPM, van Gunsteren WF, DiNola A, Haak JR. Molecular dynamics with coupling to an external bath. J Chem Phys 1984;81:3684–90.
[80] Tenney CM, Cygan RT. Molecular simulation of carbon dioxide, brine, and clay mineral interactions and determination of contact angles. Environ Sci Technol 2014;48:2035–42.
[81] Phan A, Stamatakis M, Koh CA, Striolo A. Wetting properties of clathrate hydrates in the presence of polycyclic aromatic compounds: evidence of ion-specific effects. J Phys Chem Lett 2022;13:8200–6.
[82] Espinoza DN, Santamarina JC. Water-CO2-mineral systems: interfacial tension, contact angle, and diffusion—implications to CO2 geological storage, vol. 46. Water Resources Research; 2010.
[83] Arif M, Barifcani A, Lebedev M, Iglauer S. Structural trapping capacity of oil-wet caprock as a function of pressure, temperature and salinity. Int J Greenh Gas Control 2016;50:112–20.
[84] Bachu S, Bennion DB. Interfacial tension between CO2, freshwater, and brine in the range of pressure from (2 to 27) MPa, temperature from (20 to 125) °C, and water salinity from (0 to 334 000) mg·L−1. J Chem Eng Data 2009;54:765–75.
[85] Doan QT, Keshavarz A, Miranda CR, Behrenbruch P, Iglauer S. Molecular dynamics simulation of interfacial tension of the CO2-CH4-water and H2-CH4-water systems at the temperature of 300 K and 323 K and pressure up to 70 MPa. J Energy Storage 2023;66:107470.
[86] Pandit SA, Bostick D, Berkowitz ML. An algorithm to describe molecular scale rugged surfaces and its application to the study of a water/lipid bilayer interface. J Chem Phys 2003;119:2199–205.
[87] Willard AP, Chandler D. Instantaneous liquid interfaces. J Phys Chem B 2010;114:1954–8.